

# Homogeneous nucleation rates for D<sub>2</sub>O in a supersonic Laval nozzle

Amjad Khan, Christopher H. Heath, Uta M. Dieregswiler,  
and Barbara E. Wyslouzil

*Department of Chemical Engineering, Worcester Polytechnic Institute, Worcester, Massachusetts 01609-2280*

Reinhard Strey

*Institut für Physikalische Chemie, Universität zu Köln, 50939 Köln, Germany*

(Received 27 March 2003; accepted 19 May 2003)

We measured the homogeneous nucleation rates of D<sub>2</sub>O in a supersonic nozzle. Small angle neutron scattering (SANS) experiments characterized the nanodroplet aerosols and yielded the number density  $N$  of particles formed. In these new SANS measurements the number densities were in the range of  $4 \times 10^{11} < N/\text{cm}^{-3} < 2 \times 10^{12}$ . We then determined the characteristic time interval corresponding to the peak nucleation rate  $\Delta t_{J_{\text{max}}}$  from conventional pressure profile measurements in the nozzle. The sensitive time is typically  $(11 \pm 3) \mu\text{s}$ . Combining these two pieces of information we obtained the nucleation rate  $J = N_{\text{NZ}}/\Delta t_{J_{\text{max}}}$ , where  $N_{\text{NZ}}$  is the number density of the aerosol in the nucleation zone. In this nozzle, the peak nucleation rate ranges between  $6 \times 10^{16}$  and  $1.2 \times 10^{17} \text{cm}^{-3} \text{s}^{-1}$  and is quite insensitive to the initial conditions of the expansion. © 2003 American Institute of Physics. [DOI: 10.1063/1.1590640]

## I. INTRODUCTION

Despite a long history of experimental<sup>1,2</sup> and theoretical investigation, accurate prediction of the nucleation rate  $J$  is still a difficult research problem even for vapor-to-liquid phase transitions.<sup>3,4</sup> On the experimental side, researchers have developed many apparatuses to study homogeneous nucleation. These include the diffusion cloud chamber,<sup>5-7</sup> laminar diffusion flow tube,<sup>8-10</sup> expansion cloud chamber,<sup>11,12</sup> piston expansion tube,<sup>13</sup> shock tube,<sup>14,15</sup> wave tube,<sup>16,17</sup> and the supersonic nozzle.<sup>18-23</sup> Each apparatus is sensitive to a nucleation rate range of about 3–5 orders of magnitude, thus, many different experimental methods are required to cover the wide range of nucleation rates, temperatures and critical cluster sizes required to truly distinguish between competing nucleation rate theories.

In our laboratory we work with both conventional supersonic Laval nozzles, i.e., nozzles that expand monotonically<sup>23-25</sup> and nozzles specially shaped to decouple nucleation from droplet growth.<sup>26</sup> During an experiment, a dilute gas mixture of a condensable vapor in a noncondensable carrier gas expands as it flows through the nozzle. In the absence of condensation, the pressure, density, and the temperature fall isentropically and cooling rates are on the order of  $10^6 \text{K/s}$ . As the gas cools, the condensable vapor quickly becomes supersaturated and particles begin to form by homogeneous nucleation. The newly formed particles grow rapidly, depleting the vapor, and thereby quenching further nucleation. Condensation releases heat to the flow and the pressure, density, and temperature of the gas mixture deviate from their isentropic values. The flow in these converging–diverging nozzles can be treated as one-dimensional, and the entire history of the expansion is easily obtained by measuring one state variable as a function of axial position. The onset of condensation is defined as that point in the flow where the state variables differ noticeably

from their isentropic values. Alternatively, onset can be defined as that point in the flow where the light scattered by the aerosol is first detected.<sup>21</sup>

The homogeneous nucleation rates found in nozzles,  $10^{14} < J/\text{cm}^{-3} \text{s}^{-1} < 10^{17}$ , are typical of those found during steam condensation in turbines, rapidly expanding gas flows,<sup>27</sup> and in highly reactive particle forming environments. The highest rates are produced in nozzles that expand monotonically, and where nucleation and condensation occur spontaneously as tightly coupled processes. Lower nucleation rates are produced using shaped nozzles<sup>26</sup> designed to quench nucleation prematurely and to separate nucleation from subsequent droplet growth. In either nozzle type, the critical clusters are small, usually containing fewer than 10 molecules. Working in this regime has the following advantages. First, because of the high nucleation rates, heterogeneous nucleation cannot compete unless the incoming gas stream is extremely contaminated with foreign particles<sup>21</sup> and so the process is truly homogeneous. Second, the data stringently test nucleation rate expressions because most of these are valid only in the limit of low supersaturation and large critical cluster sizes.<sup>3,4</sup> Third, the high nucleation rates and small critical cluster sizes should make our data more amenable to researchers trying to simulate nucleation processes directly using computational methods.<sup>28-30</sup>

Many researchers have used pressure trace or light scattering experiments to locate the onset of condensation in supersonic nozzles. Figure 1 summarizes the data<sup>22,24,31-34</sup> for light water, H<sub>2</sub>O, on a  $\log p$  versus  $T$  or Wilson plot. In spite of the fact that the data come from many different sources, using different nozzles and definitions of onset, all of the points appear tightly clustered around the same curve. Although these data are useful and interesting, they do not directly yield quantitative information about nucleation rates in nozzles because onset depends on a combination of nucleation and droplet growth.

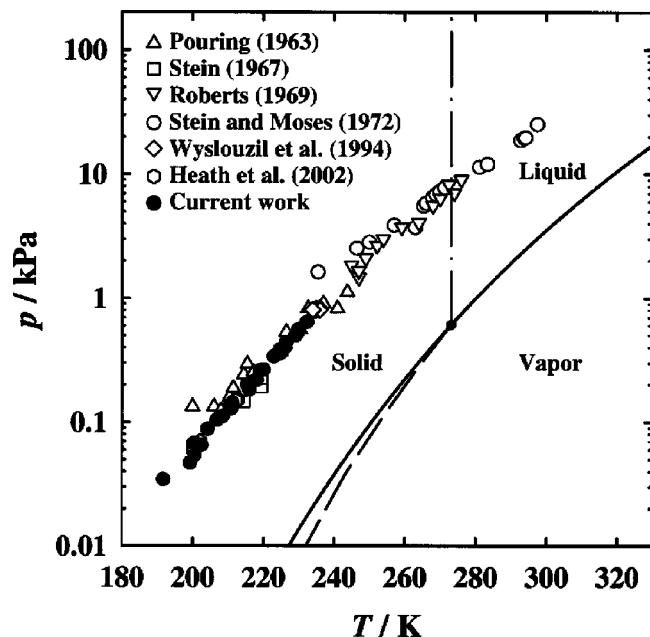


FIG. 1. The onset data for H<sub>2</sub>O from previous supersonic nozzle experiments (Refs. 22, 24, and 31–34) is compared to the current data. The solid line is the vapor–liquid equilibrium curve for H<sub>2</sub>O, the dashed line is the solid–vapor equilibrium boundary and the dash–dotted line is the solid–liquid equilibrium line. The data from Heath *et al.* (Ref. 24) lie directly underneath the current measurements.

Over the past 20 years, the major thrust in nucleation research has been to extract quantitative nucleation rates directly from experimental data.<sup>2,12</sup> For supersonic nozzles this goal was achieved only very recently by Streletzky *et al.* using specially shaped nozzles.<sup>26</sup> There, the nozzle shape largely determined the characteristic time for droplet formation and small angle neutron scattering (SANS) experiments provided the aerosol number density. Combining these two pieces of information yielded the nucleation rate as a function of supersaturation and temperature. In this paper we extend the work of Streletzky *et al.* to extract peak nucleation rates during condensation in a conventional Laval nozzle. The analysis methods developed here were recently used by Heath *et al.*<sup>25</sup> to estimate H<sub>2</sub>O–D<sub>2</sub>O binary nucleation rates in the same nozzle.

At this time the limiting step to measuring nucleation rates in supersonic nozzles is the time required to collect the SANS data for these weakly scattering systems. For example, the current experiments required up to 4 h to adequately characterize each aerosol sample, and, thus, the total number of conditions investigated was limited to 7. Modeling work by Heath and co-workers<sup>35</sup> suggested that the peak nucleation rates depend somewhat on the stagnation conditions and the location of the onset of condensation in this nozzle. We therefore chose our operating conditions in order to (1) maintain the onset at two fixed positions in the nozzle starting from different stagnation temperatures, (2) maintain the same onset temperature in the nozzle starting from different stagnation temperatures, and (3) maintain the same stagnation temperature but varying the onset position along the nozzle. Extensive pressure trace experiments with both H<sub>2</sub>O and D<sub>2</sub>O characterized the condensation of these

two species as a function of the operating parameters. Finally, the pressure trace results and the SANS results were combined to obtain the peak nucleation rates in a conventional supersonic nozzle.

Although H<sub>2</sub>O nucleation and condensation is more relevant to practical applications, H<sub>2</sub>O has a much weaker neutron scattering length density than D<sub>2</sub>O. For identical aerosol size distribution parameters, a D<sub>2</sub>O aerosol has a scattering signal that is ~130 times stronger than that for H<sub>2</sub>O. Thus, all of the SANS experiments were conducted using D<sub>2</sub>O although extensive pressure trace measurements were made for both isotopes of water. Parallel work by Heath *et al.*<sup>25</sup> and Wölk and Strey<sup>36</sup> suggests, however, that one can predict the nucleation rates for H<sub>2</sub>O based on the D<sub>2</sub>O results rather precisely.

The paper is organized as follows: In the Experimental section we briefly describe the apparatus, the pressure trace experiments and associated analyses, the SANS experiments and interpretation of the scattering data, and the theoretical framework for extracting the nucleation rates from the measurements. In the Results and Discussion we give the detailed results of the pressure trace and SANS experiments, and the peak nucleation rates derived from these measurements. Finally we present our conclusions.

## II. EXPERIMENT

### A. Apparatus

All of our experiments were conducted using a conventional Laval nozzle,<sup>23–25</sup> with a nominal opening angle of approximately 1.8° and a nominal throat area  $A^*$  of 63.5 mm<sup>2</sup>. The sidewalls of the nozzle contain thin Si-windows that are transparent to the neutrons for the SANS experiments. Two slightly different flow arrangements were used to produce the aerosols. All of the H<sub>2</sub>O experiments were conducted using the setup described by Heath *et al.*<sup>24,25</sup> There, the main carrier gas flow was produced by flowing liquid N<sub>2</sub> from a low pressure dewar to an external heat exchanger where it was vaporized and brought up to room temperature. All the D<sub>2</sub>O experiments were conducted using the set up illustrated in Fig. 2 where the main flow of the carrier gas was supplied by directly drawing from the gas side of two high pressure liquid nitrogen (LN<sub>2</sub>) dewars. Inline heaters then raised the temperature of the gas to ambient conditions. In addition to simplifying the operation, this change also reduced pressure oscillations in the system significantly.

As illustrated in Fig. 2, carrier gas from the two high pressure (1.5 MPa) LN<sub>2</sub> dewars enters the ballast tank, flows through a high volume filter, and is then mixed with a second stream of carrier gas that is rich in the condensible vapor. To produce the vapor-rich stream, the condensible material is fed as a liquid into a vaporizer using a peristaltic pump and forced through a spray nozzle along with a heated N<sub>2</sub> gas stream. The droplets mix with and evaporate in a second heated N<sub>2</sub> gas stream. The N<sub>2</sub> for these two streams is provided by the third LN<sub>2</sub> dewar.

The combined gas mixture then flows through the water bath that controls the stagnation temperature of the system. The relative humidity (RH) of the mixture is monitored using

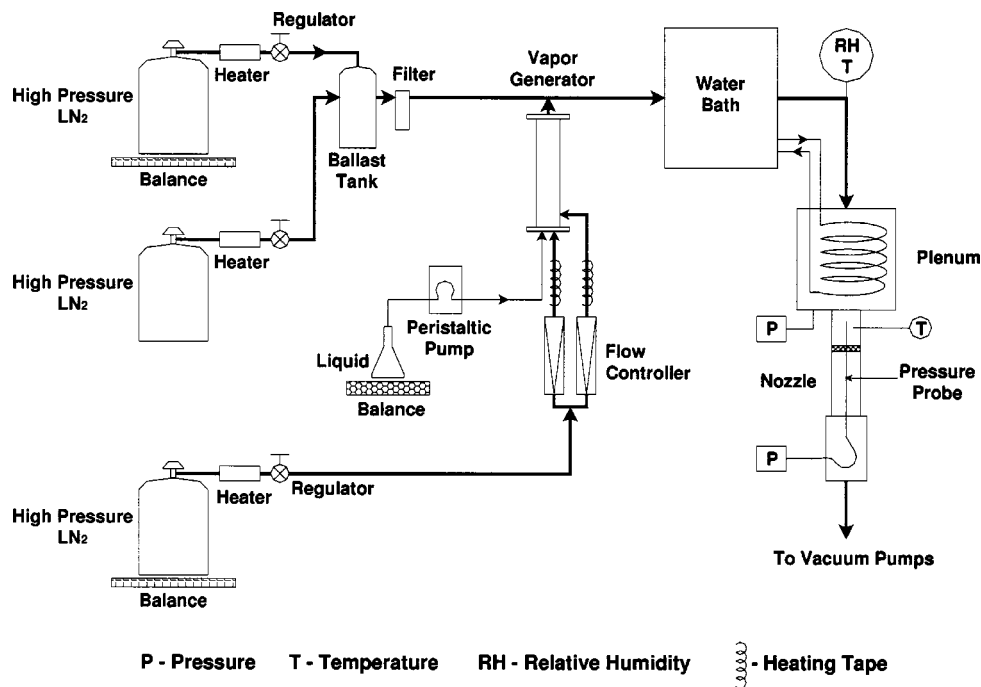


FIG. 2. A simple schematic diagram of the equipment. The major difference between the current setup and the previous one is that all of the carrier gas is now drawn directly from the gas side of identical high pressure LN<sub>2</sub> dewars.

a RH meter and the gas mixture then flows through the plenum. The plenum contains additional finned copper coils to make the final temperature adjustment and the pressure is measured here. An additional measurement of the nonisentropic pressure losses between the plenum and the entrance to the nozzle is made in a separate experiment using a stagnation pressure probe. These losses are subtracted from the plenum pressure to obtain the true stagnation pressure,  $p_0$ . The mixture then enters the flow straightener where the stagnation temperature,  $T_0$ , is recorded using a Class A RTD probe. As the gas mixture enters the nozzle, it starts to expand and cool. The temperature falls, the supersaturation of the condensable vapor increases rapidly, and particle production begins. The supersaturation continues to increase until enough particles have formed so that rapid particle growth depletes the vapor and new particle formation stops. Finally, the gas stream exits the nozzle and is pumped out of the system using two vacuum pumps.

### B. Pressure trace measurements

Once the system reaches steady state, we record the static pressure as a function of position,  $x$ , along the centerline of the nozzle using a 0.9 mm diam probe. Pressure measurements are made at 0.1 mm intervals in the vicinity of the throat and at 1 mm intervals downstream of the throat, until the end of the nozzle is reached.

Before conducting experiments with condensible substances, we determine the effective shape or area ratio of the nozzle by measuring the dry pressure trace (i.e., the expansion of N<sub>2</sub> carrier gas only) at the desired  $p_0$  and  $T_0$ . We then use the effective area ratio, the pressure trace measurements for a condensible mixture at fixed stagnation conditions, and an equation of state, as input to a data reduction

code that integrates the diabatic flow equations<sup>23</sup> to obtain the temperature,  $T$ , density,  $\rho$ , velocity,  $v$ , and the condensate mass fraction,  $g$ , at every measured point,  $x$ , in the nozzle. Because the mixtures are dilute, the initial composition of the gas stream is given by

$$y \cong \frac{\dot{m}_v / \mu_v}{\dot{m}_i^0 / \mu_i}, \quad (1)$$

where  $y$  is the mole fraction of the condensible species,  $\dot{m}_v$  and  $\mu_v$  are the mass flow rate and molecular weight of the condensible species,  $\dot{m}_i^0$  is the mass flow rate of pure nitrogen through the nozzle, and  $\mu_i$  is the molecular weight of the inert carrier gas. The value of  $\dot{m}_i^0$  is determined by measuring the amount of nitrogen that flows through the nozzle over the course of 1 h at a fixed  $p_0$  and  $T_0$ . From the value of  $\dot{m}_i^0(p_0, T_0)$  we can also determine the area of the throat  $A^*$  by mass balance.

Finally, the partial pressure of the condensible vapor  $p_v$  depends on the initial condensible partial pressure  $p_{v,0} = yp_0$ , the local pressure ratio, and the fraction of material condensed  $g/g_\infty$ , as

$$p_v = p_{v,0} \left( \frac{p}{p_0} \right) \left( 1 - \frac{g}{g_\infty} \right), \quad (2)$$

where  $g_\infty = \dot{m}_v / \dot{m}_i$ . Thus, the supersaturation profile  $S(x)$  is given by,

$$S = \frac{p_v}{p^\infty(T)}, \quad (3)$$

where  $p^\infty(T)$  is the equilibrium vapor pressure of the condensible.

## C. SANS

### 1. Setup

The SANS experiments were conducted using the NG7-SANS instrument at the NIST Center for Neutron Research (NCNR) of the National Institute of Standards and Technology (NIST), Gaithersburg, Maryland. For the SANS experiments, the nozzle and the plenum were placed in the sample box with the neutron beam oriented perpendicular to the aerosol stream. The silicon and sapphire windows that usually separate the sample chamber from the detector tube and the neutron guide were removed to reduce and stabilize the background scattering, and the sample box was evacuated. During the experiments the pressure in the entire neutron flight path was less than 12 Pa and varied by less than a few percent. A 1.2 cm wide and 0.4 cm high Gadolinium aperture, centered 5.6 cm downstream of the nozzle throat, and the 1.27 cm width of the nozzle define the  $\sim 0.6$  cm<sup>3</sup> scattering volume. After passing through the nozzle, the neutrons scattered by the aerosol were recorded on a two-dimensional detector consisting of a 128×128 array of 0.25 cm<sup>2</sup> <sup>3</sup>He detectors.

The static pressure probe is not in place during the SANS experiments. Although removing the 0.9 mm diam probe increases  $A^*$  by about 1%, the area downstream of the throat also increases, and the actual change in the expansion rate is less than 0.6%. Hence, we assume that the condensation process during the pressure trace and SANS experiments is the same.

The SANS experiments were conducted at an average neutron wavelength of  $\lambda=0.8$  nm, a wavelength spread of  $\Delta\lambda=22\%$ , and sample-to-detector distances (SDD) of 2.0 m and 3.75 m. The neutron scattering measurements were normally made in 30 min intervals, and scattering from an aerosol sample was followed by a 30 min background measurement of pure nitrogen flowing through the nozzle.

### 2. SANS data analysis

The two-dimensional SANS data were corrected by subtracting the background scattering signal from the flow of pure nitrogen in the nozzle. The sensitivity of the individual detector cells was accounted for by dividing the intensities by those from a water sample on a pixel-by-pixel basis. The data were placed on an absolute intensity scale, and a standard mask was applied. We used the SANS data reduction software provided by NIST to produce the one-dimensional scattering intensity  $I(q)$ , where  $q$  is the momentum transfer wave vector.<sup>37</sup> In performing the radial average we accounted for a Doppler shift in the data that arises because the velocity of the droplets is about 90% of that of the neutrons.<sup>38–40</sup> To make the correction<sup>41</sup> we used the velocity of the aerosol droplets derived from the pressure trace information and assumed that the droplets move at the same speed as the gas. For experiments with two sample-to-detector distances (SDD) the spectra were combined without any additional adjustments for an overall  $q$  range of  $0.09 < q < 1.8$  nm<sup>-1</sup>.

### 3. Fitting the spectra

To determine the parameters of the aerosol size distribution from the  $I(q)$  versus  $q$  scattering spectrum, we assume that the aerosol has a lognormal size distribution with a median droplet radius  $r_g$ , a distribution width parameter  $\ln \sigma_r$ , a volume fraction  $\phi$ , and a difference in scattering length density  $\Delta\rho$ . The synthetic scattering intensity,  $I_s$ , is given by

$$I_s(q) = \frac{3\phi}{4\pi\langle r^3 \rangle} \frac{1}{\ln \sigma_r \sqrt{2\pi}} \int_0^\infty \frac{1}{r} \times \exp\left[-\frac{(\ln r - \ln r_g)^2}{2 \ln^2 \sigma_r}\right] P(q,r) dr, \quad (4)$$

where the particle form factor for spherical particles is given by

$$P(q,r) = \frac{16\pi^2(\Delta\rho)^2(\sin qr - qr \cos qr)^2}{q^6}. \quad (5)$$

We use a nonlinear fitting program to minimize the difference between the experimental and synthetic scattering spectra. This program takes both the uncertainty in the data and the resolution of the SANS instrument into account. Because  $\phi$  and  $\Delta\rho$  are perfectly correlated we first set  $\Delta\rho = 6.39 \times 10^{10}$  cm<sup>-1</sup>, the scattering length density<sup>42</sup> of D<sub>2</sub>O, and let  $\phi$  vary. Once the fit has converged, we calculate the number density using

$$N = \frac{3\phi_{\text{SANS}}}{4\pi\langle r^3 \rangle}, \quad (6)$$

where  $\phi_{\text{SANS}}$  is the volume fraction derived by fitting the SANS spectrum and  $\langle r^3 \rangle$  is the third moment of the size distribution. We also derive a second estimate for  $N$  by using the volume fraction obtained from the pressure traces  $\phi_{\text{PT}}$  in Eq. (10). This approach is equivalent to letting  $\Delta\rho$  rather than  $\phi$  vary.

### D. Estimating the peak nucleation rates

To estimate the peak nucleation rates as a function of supersaturation and temperature, i.e.,  $J_{\text{max}}(S_{J_{\text{max}}}, T_{J_{\text{max}}})$ , we need the number density of the aerosol,  $N$ , and the time interval over which the aerosol is formed. The value of  $N$  comes from fitting the SANS spectrum as described above. The characteristic time,  $\Delta t_{J_{\text{max}}}$ , comes from an analysis of the supersaturation and temperature profiles obtained from the pressure trace experiments.

As in laminar flow experiments,<sup>8,9,43</sup> we assume that the ratio of the max nucleation rate  $J_{\text{exp}}^{\text{max}}$  to the particle production rate  $\int J_{\text{exp}} dV$  is the same for the experiments as that predicted by any reasonable nucleation theory. If this is true, then

$$\frac{J_{\text{exp}}^{\text{max}}}{\int J_{\text{exp}} dV} = \frac{J_{\text{theory}}^{\text{max}}}{\int J_{\text{theory}} dV} = \frac{1}{V_{J_{\text{max}}}}, \quad (7)$$

where  $V_{J_{\text{max}}}$  is the characteristic volume corresponding to the maximum nucleation rate. To evaluate the integrals in Eq. (7),  $dV$  is set equal to  $A dx$ , where  $A(x)$  is derived from the

TABLE I. The stagnation and onset conditions for the H<sub>2</sub>O condensation experiments.

Stagnation conditions				Onset conditions			
$p_0$ , kPa	$T_0$ , °C	$\dot{m}_v$ , g/min	$p_{v0}$ , Pa	$p/p_0$	$p_v$ , Pa	$T_{on}$ , K	$x_{on}$ , cm
$T_0 = 13.5 \pm 0.1$ °C							
59.68	13.50	0.776	142.2	0.2426	34.5	191.7	5.17
59.67	13.49	1.301	238.4	0.2831	67.5	200.3	3.63
59.62	13.49	1.789	327.6	0.3167	103.8	206.8	2.64
59.63	13.50	2.711	496.5	0.3694	183.4	216.1	1.53
$T_0 = 25 \pm 0.1$ °C							
59.65	25.00	1.038	193.6	0.2421	46.9	199.2	5.22
59.60	24.98	1.786	332.9	0.2637	87.8	204.2	4.33
59.65	25.00	2.584	481.9	0.2969	143.1	211.2	3.21
59.77	24.99	4.136	772.7	0.3377	261.0	219.1	2.17
59.71	25.00	6.197	1156.8	0.3789	438.3	226.5	1.40
59.72	25.02	8.307	1551.1	0.4146	643.2	232.4	0.91
$T_0 = 35 \pm 0.1$ °C							
59.68	35.00	1.303	246.8	0.2207	54.5	200.6	6.33
59.66	35.00	2.598	491.7	0.2634	129.5	211.0	4.33
59.69	35.00	3.920	742.3	0.2957	219.5	218.1	3.25
59.65	35.00	6.210	1175.3	0.3287	386.3	224.8	2.39
59.66	34.99	8.317	1574.4	0.3554	559.6	229.9	1.83
$T_0 = 45 \pm 0.1$ °C							
59.73	45.02	1.671	321.9	0.2040	65.7	202.5	7.36
59.68	45.02	2.572	495.0	0.2259	111.8	208.5	6.06
59.65	45.01	2.961	569.6	0.2333	132.9	210.4	5.69
59.68	45.02	4.113	791.5	0.2532	200.4	215.5	4.78
59.68	45.01	5.061	973.9	0.2729	265.8	220.1	4.00
59.66	45.02	6.189	1190.6	0.2852	339.6	223.0	3.59
59.73	45.00	6.982	1344.9	0.3000	403.5	226.2	3.13
59.66	45.02	8.275	1592.0	0.3133	498.8	229.0	2.77
59.63	45.01	8.762	1684.9	0.3163	532.9	229.7	2.70
59.68	45.01	5.061	973.9	0.2729	265.8	220.1	4.00

experimentally determined values of the area ratio ( $A(x)/A^*$ ) and  $A^*$ . The characteristic time corresponding to  $J_{max}$  comes directly from  $V_{J_{max}}$  and the volumetric flow rate in the nucleation zone,  $\dot{V}_{NZ}$  since

$$\Delta t_{J_{max}} = \frac{V_{J_{max}}}{\dot{V}_{NZ}}, \quad (8)$$

where

$$\dot{V}_{NZ} = \dot{m} / \rho_{NZ}. \quad (9)$$

In Eq. (9)  $\dot{m} = \dot{m}_v + \dot{m}_i$  is the mass flow rate through the nozzle and  $\rho_{NZ}$  is the density of the gas in the nucleation zone. Finally, the peak nucleation rate is

$$J_{max}(S_{J_{max}}, T_{J_{max}}) = \frac{N}{\Delta t_{J_{max}}} \times \frac{\rho_{NZ}}{\rho_{vv}} = \frac{N\dot{m}}{\rho_{vv}V_{J_{max}}}, \quad (10)$$

where  $\rho_{vv}$  is the density in the viewing volume, and the factor  $\rho_{NZ}/\rho_{vv}$  corrects for the continued expansion of the gas between the nucleation zone and observation region. By using the value of  $N$  from the SANS measurements, we assume that all the droplets were formed in the nucleation zone and that coagulation between the nucleation zone and viewing volume is negligible. For the current nozzle these assumptions are both valid.

TABLE II. The stagnation and onset conditions for D<sub>2</sub>O condensation experiments conducted prior to NIST without insulation around the flow straightener. The experiments marked with the following symbol • are outliers. They have been omitted from Fig. 3 and were not included in the fit.

Stagnation conditions				Onset conditions			
$p_0$ , kPa	$T_0$ , °C	$\dot{m}_v$ , g/min	$p_{v0}$ , Pa	$p/p_0$	$p_v$ , Pa	$T_{on}$ , K	$x_{on}$ , cm
$T_0 = 25 \pm 0.1$ °C							
•59.69	24.99	0.849	142.3	0.2209	31.4	194.1	6.29
59.65	25.00	1.273	213.2	0.2496	53.2	201.0	4.89
59.65	25.01	1.550	259.6	0.2650	68.8	204.4	4.27
59.70	25.00	1.964	329.2	0.2844	93.6	208.6	3.58
59.70	24.99	2.547	995.4	0.3907	388.9	228.4	1.22
59.73	25.02	2.973	427.2	0.3128	133.6	214.4	2.76
59.67	24.99	3.963	498.2	0.3215	160.2	216.0	2.54
59.70	25.01	4.955	664.3	0.3519	233.8	221.7	1.88
59.73	25.01	5.938	831.0	0.3705	307.9	225.0	1.53
$T_0 = 35 \pm 0.1$ °C							
•59.69	34.98	0.989	168.5	0.2061	34.7	196.7	7.20
59.72	34.99	1.973	336.3	0.252	84.8	208.4	4.79
59.73	34.99	2.954	503.7	0.2810	141.5	214.9	3.71
59.72	35.00	3.926	669.3	0.3025	202.4	219.5	3.05
59.66	35.02	5.065	862.8	0.3232	278.8	223.7	2.50
59.66	35.00	6.056	1031.3	0.3380	348.6	226.6	2.16
59.67	35.00	7.064	1203.2	0.3552	427.4	229.8	1.81
59.69	35.01	8.012	1365.3	0.3657	499.3	231.8	1.62
$T_0 = 45 \pm 0.1$ °C							
59.67	44.99	4.055	701.9	0.2619	183.8	217.5	4.40
59.67	45.03	5.126	887.4	0.2793	247.8	221.6	3.78
59.66	44.97	6.132	1061.3	0.2963	314.5	225.3	3.24
59.72	44.96	8.125	1407.6	0.3149	443.2	229.3	2.73
59.71	45.00	9.112	1579.8	0.3253	514.0	231.5	2.47
59.69	45.00	9.980	1728.1	0.3341	577.3	233.3	2.27

## E. Materials and physical properties

The D<sub>2</sub>O (Sigma Aldrich) had more than 99.9% D substitution. The deionized H<sub>2</sub>O used for these experiments had resistivity values greater than 15 MΩ. The thermophysical parameters of light and heavy water used to invert the pressure trace data, as well as calculate the supersaturation profiles and the nucleation rates, are those compiled by Wölk and Strey<sup>36</sup> and also given in Heath *et al.*<sup>24,25</sup>

## III. RESULTS AND DISCUSSION

### A. Pressure trace results

Because the nozzle was never disassembled, the effective nozzle expansion rate [ $d(A/A^*)/dx = 0.0477 \pm 0.0001 \text{ cm}^{-1}$ ] and N<sub>2</sub> molar flow rate (17.8 mol min<sup>-1</sup> at  $p_0 = 59.6 \pm 0.2 \text{ kPa}$ ,  $T_0 = 298.16 \text{ K}$ ) measured before and after the SANS experiments were identical. As in our earlier work, the onset of condensation is defined as that point in the flow where the condensing flow temperature,  $T_{cf}$ , is 0.5 K higher than the temperature of the isentropic expansion of the mixture  $T_{mi}$ . Table I summarizes the stagnation and onset conditions obtained for H<sub>2</sub>O, while Tables II, III, and IV summarize the results for D<sub>2</sub>O. The experiments for H<sub>2</sub>O were conducted at four different stagnation temperatures,  $T_0 = 13.5$  °C, 25 °C, 35 °C, and 45 °C, while the D<sub>2</sub>O experi-

TABLE III. The stagnation and onset conditions for D<sub>2</sub>O condensation experiments conducted prior to NIST with insulation around the flow straightener.

Stagnation conditions				Onset conditions			
$p_0$ , kPa	$T_0$ , °C	$\dot{m}_v$ , g/min	$p_{v0}$ , Pa	$p/p_0$	$p_v$ , Pa	$T_{on}$ , K	$x_{on}$ , cm
$T_0 = 25 \pm 0.1$ °C							
59.74	25.00	1.828	306.6	0.2765	84.8	206.9	3.82
59.75	25.01	2.915	489.1	0.3147	153.9	214.7	2.69
59.74	25.01	4.360	731.3	0.3518	257.3	221.7	1.86
$T_0 = 35 \pm 0.1$ °C							
59.71	35.00	3.207	546.6	0.2814	153.8	215.0	3.67
59.75	35.02	4.933	841.4	0.3173	267.0	222.5	2.63
59.75	35.00	7.511	1281.1	0.3511	449.8	229.1	1.88
$T_0 = 45 \pm 0.1$ °C							
59.74	44.99	5.407	937.1	0.2784	260.9	221.4	3.76
59.68	45.00	6.0823	1053.0	0.2912	306.7	224.3	3.37
59.67	45.05	8.592	1487.3	0.3151	468.7	229.5	2.69
59.77	45.00	13.107	2272.8	0.3491	793.5	236.4	1.92
59.70	45.01	13.729	2378.0	0.3597	855.4	238.4	1.73
59.72	45.01	13.924	2412.1	0.3576	862.6	238.0	1.76

ments were conducted at the three higher temperatures only. The stagnation pressure,  $p_0$ , was constant at  $59.6 \pm 0.2$  kPa for all of the experiments.

The current H<sub>2</sub>O data set was already presented in Fig. 1. Onset temperatures range from 192 K to 232 K, and over this temperature range the onset pressures are an exponential function of temperature. Only a few of the onset values at lower temperatures deviate from the exponential trend. In most of the experiments that deviate, the flow rates are low, little heat is added to the flow, and onset is 5–7 cm downstream from the throat. In general, these create the most difficult conditions to determine onset. Overall, the data are tightly clustered about a single line and there is no significant

TABLE IV. The stagnation and onset conditions for the D<sub>2</sub>O condensation experiments conducted after NIST with insulation around the flow straightener. The experiments marked with the \* correspond closely to the SANS experiments and the pressure profiles from these experiments are shown in Fig. 4.

Stagnation conditions				Onset conditions			
$p_0$ , kPa	$T_0$ , °C	$\dot{m}_v$ , g/min	$p_{v0}$ , Pa	$p/p_0$	$p_v$ , Pa	$T_{on}$ , K	$x_{on}$ , cm
$T_0 = 25 \pm 0.1$ °C							
*59.70	24.98	1.909	320.1	0.2817	90.2	208.0	3.65
59.70	25.00	2.023	339.1	0.2885	97.8	209.5	3.42
59.72	24.99	4.405	738.6	0.3554	262.5	222.3	1.79
59.73	24.99	4.455	747.2	0.3569	266.7	222.6	1.76
*59.78	25.00	4.504	756.0	0.3574	270.2	222.8	1.75
59.66	25.00	4.523	757.7	0.3616	274.0	223.4	1.67
$T_0 = 35 \pm 0.1$ °C							
*59.65	35.00	3.242	552.0	0.2820	155.7	215.1	3.65
*59.69	35.01	5.100	868.9	0.3196	277.7	223.0	2.58
*59.61	35.00	7.707	1311.3	0.3582	469.8	230.4	1.75
$T_0 = 45 \pm 0.1$ °C							
*59.66	45.00	5.733	992.2	0.2809	278.7	222.0	3.71
59.65	44.99	5.786	1001.2	0.2821	282.4	222.2	3.68
59.72	44.99	5.906	1023.2	0.2852	291.8	222.9	3.56
59.63	45.01	6.266	1083.8	0.2927	317.3	224.6	3.33
*59.70	44.99	13.282	2300.3	0.3586	824.8	238.1	1.75

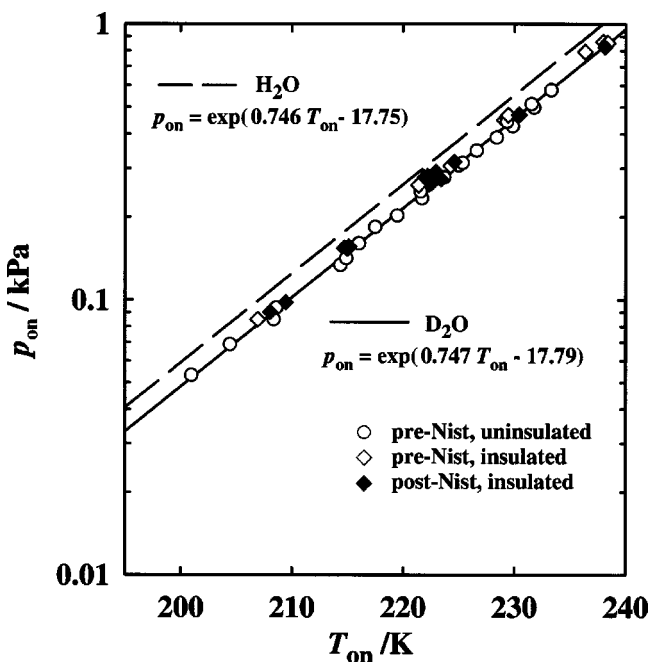


FIG. 3. The onset data for D<sub>2</sub>O measured before and after the NIST experiments and with and without insulation. The exponential fit functions are included for both the H<sub>2</sub>O and the D<sub>2</sub>O data.

trend with respect to the stagnation temperature. The current data set lies directly on top of the earlier results of Health *et al.*<sup>24</sup>

The results of the pressure traces experiments with D<sub>2</sub>O are presented in three different tables. Table II summarizes

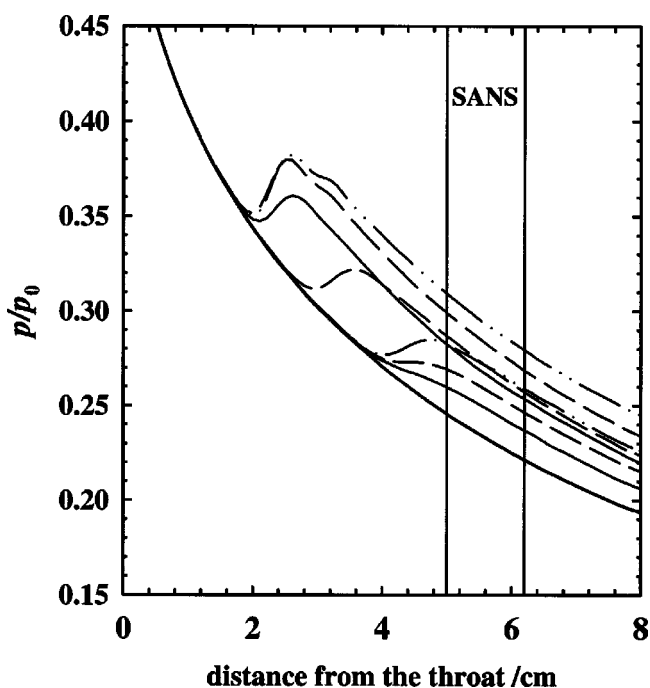


FIG. 4. The D<sub>2</sub>O pressure profiles corresponding to the SANS experiments are as follows. The lowest solid curve is the dry isentropic expansion (N<sub>2</sub> only). For the condensing flows, the solid lines correspond to expansions starting from  $T_0 = 25$  °C, the dashed lines correspond to expansion starting from  $T_0 = 35$  °C, and the dash-dotted lines correspond to expansions starting from  $T_0 = 45$  °C. The actual flow rates and initial partial pressures are summarized in Table IV and are marked with the \* symbol. The vertical lines indicate the location of the SANS viewing volume.

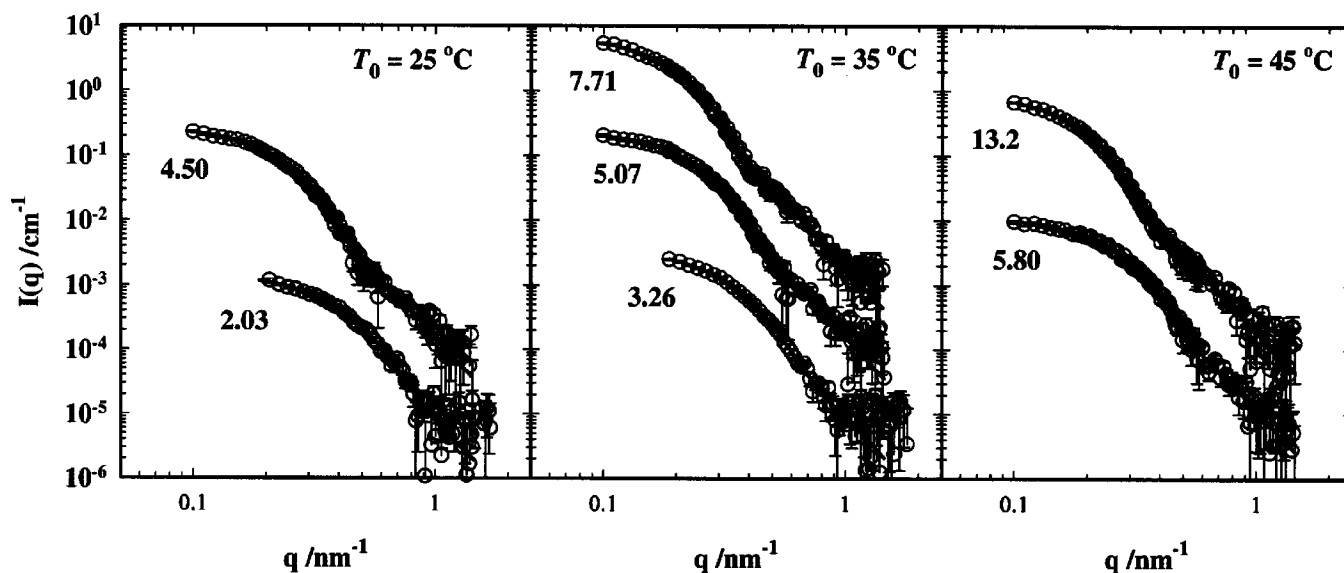


FIG. 5. The SANS spectra of the nanodroplet aerosol. The average mass flowrates of the condensable vapor, in g/min, is noted to the left and slightly below each curve. The spectrum with the lowest intensity is on the absolute scale. The other spectra are offset by factors of 10 or 100, respectively.

those pressure trace experiments that were conducted prior to the SANS experiments without insulation on the flow straightener. The values in Tables III and IV correspond to the experiments with insulation on the flow straightener conducted prior to and after the SANS experiments, respectively. Insulation was added in order to cut down on heat transfer to the surroundings, and to improve the accuracy of the temperature measurements. The effect of the added insulation was discussed in detail by Heath *et al.*<sup>24</sup> and will not be repeated here. The experiments done before the SANS experiments established the optimal operating conditions, while those conducted after the SANS measurements confirmed that there were no changes due to transporting the equipment from WPI to the SANS facility at the NIST.

The Wilson plot in Fig. 3 summarizes the D<sub>2</sub>O onset data found in Tables II–IV. Again the onset pressures are an exponential function of onset temperature. The open diamonds represent the onset data points for D<sub>2</sub>O before the SANS experiments, the filled diamonds represent the onset data points after the SANS experiments and the open circles represent the onset data points taken without insulation around the flow straightener. The exponential fit function for the H<sub>2</sub>O data is also included on this figure and over the experimental temperature range the two lines are almost parallel.

Our goal was to choose operating conditions for the SANS experiments so that (1) onset occurred at a fixed position in the nozzle starting from three different stagnation temperatures, (2) onset occurred at the same temperature in the nozzle starting from three different stagnation temperatures, and (3) onset occurred at three different positions in the nozzle with  $T_0$  fixed. Figure 4 illustrates the pressure traces corresponding as closely as possible to the conditions used during the SANS experiments. These are the conditions marked with the \* symbol in Table IV.

For each value of  $T_0$ , we obtained onset  $\sim 1.75$  cm and  $\sim 3.65$  cm downstream of the throat. For  $T_0 = 35$  °C, onset occurred at three different positions in the nozzle. Finally, experiments with stagnation temperatures and flow rates of  $(T_0, \dot{m}_v) = (25, 4.405)$ ,  $(35, 5.100)$ , and  $(45, 5.733)$  (°C, g/min) all had onset occurring very close to 222 K.

## B. SANS experimental results

Figure 5 shows the combined  $I(q)$  versus  $q$  SANS spectra for the three different values of  $T_0$ . For clarity, at each  $T_0$  the spectrum corresponding to the lowest partial pressure is shown at its true absolute intensity while those at higher partial pressures are offset by factors of 10 or 100. When we made measurements at multiple sample-to-detector dis-

TABLE V. The size distribution parameters for D<sub>2</sub>O derived from the SANS spectra. The values of  $N$  in column 6 and column 8 are calculated using Eq. (10) with  $\phi_{\text{SANS}}$  and  $\phi_{\text{PT}}$ , respectively.

$T_0$	$\dot{m}_v$ , g/min	$r_g$ , Å	$\ln \sigma_r$	$\phi_{\text{SANS}}$	$N, \text{cm}^{-3}$	$\phi_{\text{PT}}$	$N, \text{cm}^{-3}$
25	2.03	43.2 ± 1.5	0.256 ± 0.018	4.91 ± 0.08 × 10 <sup>-7</sup>	1.02 × 10 <sup>12</sup>	7.4 × 10 <sup>-7</sup>	1.51 × 10 <sup>12</sup>
	4.50	84.2 ± 0.5	0.203 ± 0.005	1.66 ± 0.01 × 10 <sup>-6</sup>	5.53 × 10 <sup>11</sup>	1.65 × 10 <sup>-6</sup>	5.53 × 10 <sup>11</sup>
35	3.26	53.4 ± 1.0	0.253 ± 0.011	6.78 ± 0.07 × 10 <sup>-7</sup>	7.98 × 10 <sup>11</sup>	1.05 × 10 <sup>-6</sup>	1.24 × 10 <sup>12</sup>
	5.07	81.1 ± 0.5	0.199 ± 0.005	1.66 ± 0.01 × 10 <sup>-6</sup>	6.23 × 10 <sup>11</sup>	1.64 × 10 <sup>-6</sup>	6.23 × 10 <sup>11</sup>
	7.71	104.1 ± 0.5	0.189 ± 0.005	2.52 ± 0.01 × 10 <sup>-6</sup>	4.53 × 10 <sup>11</sup>	2.37 × 10 <sup>-6</sup>	4.26 × 10 <sup>11</sup>
45	5.8	70.3 ± 0.8	0.216 ± 0.007	1.11 ± 0.01 × 10 <sup>-6</sup>	6.18 × 10 <sup>11</sup>	1.56 × 10 <sup>-6</sup>	8.69 × 10 <sup>11</sup>
	13.2	111.9 ± 0.6	0.181 ± 0.005	2.81 ± 0.01 × 10 <sup>-6</sup>	4.13 × 10 <sup>11</sup>	2.73 × 10 <sup>-6</sup>	4.01 × 10 <sup>11</sup>

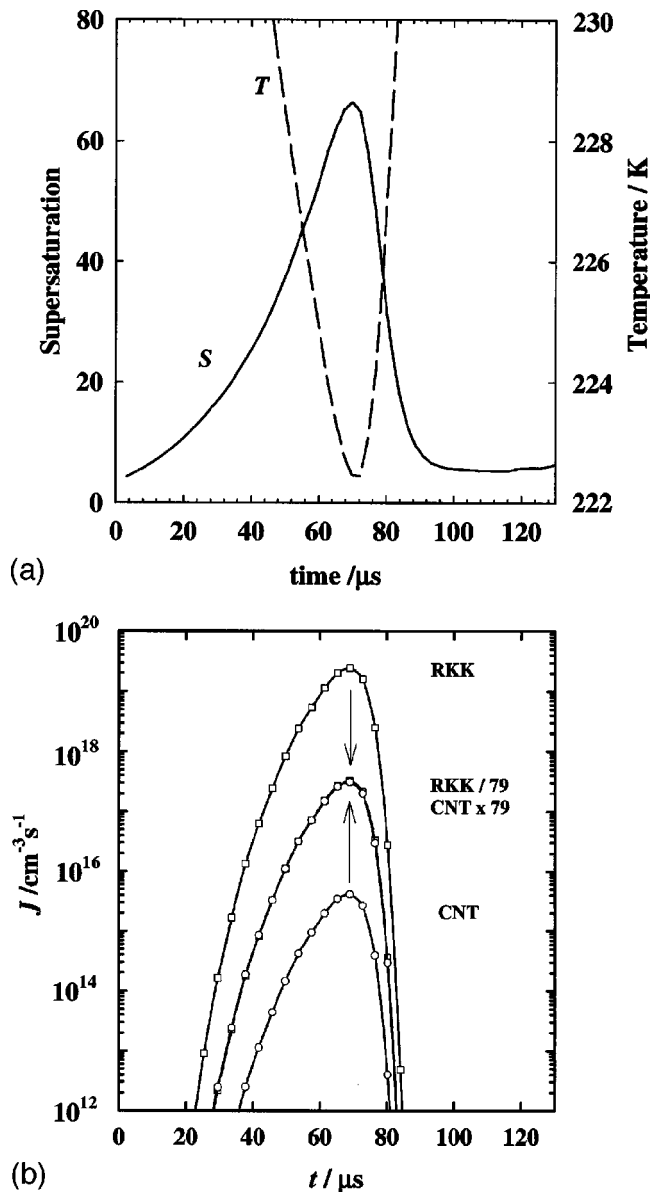


FIG. 6. (a) The supersaturation and temperature in the nozzle are illustrated as function of time for initial temperature  $T_0=308$  K, pressure  $p_0=59.6$  kPa and vapor pressure  $p_{v,0}=0.89$  kPa. (b) The nucleation rates predicted by classical nucleation theory (Ref. 44) (CNT) and the Reiss Katz and Kegel theory (Ref. 45) (RKK) were calculated using the temperature and supersaturation profiles given in (a). Note that the two curves overlap exactly when each is scaled by an appropriate factor.

tances, the absolute intensities for each sample-to-detector distance (SDD) were determined independently and no further corrections were made. Each spectrum has an inflection point followed by a  $q^{-4}$  Porod decay characteristic of scattering by homogenous spherical particles. As the initial condensable vapor pressure  $p_{v,0}$  increases, the inflection point shifts to lower  $q$ , indicating an increase in the droplet size.

We obtained the best-fit parameters to the aerosol size distribution assuming a log-normal distribution of droplets using the procedures outlined in Sec. II C 3. Although they are difficult to see, the best-fit curves are included in Fig. 5.

Table V summarizes the size distribution parameters obtained by fitting the SANS spectra. At fixed  $T_0$ , the mean radius of the particles increases with the flow rate of the

condensable and as onset moves upstream in the nozzle. This observation is consistent with the change in the location of the inflection point in the SANS spectra noted above. Although the observed particle size is primarily a function of the amount of condensable added to the flow, the time available for particle growth between the nucleation zone and the viewing volume can also be important. Again at fixed  $T_0$ , the number density of the particles with larger mean diameter is less than that of the particles with smaller mean diameter, and in general, aerosols formed earlier in the nozzle are more monodisperse in the sense that  $\ln \sigma_r$  has a lower value. The error bars increase for experiments with onset at the furthest position downstream in the nozzle ( $\sim 3.65$  cm) because the volume fraction of the sample is the lowest and the resultant scattering signal is the weakest. All of the error bars quoted in Table V correspond to one standard deviation in the value of each parameter with the other parameters held at their optimal values.

### C. Peak nucleation rates of D<sub>2</sub>O

In order to estimate the peak nucleation rates  $J_{\max}(S_{J_{\max}}, T_{J_{\max}})$ , we still need to determine the characteristic time  $\Delta t_{J_{\max}}$  as well as the values of  $S_{J_{\max}}$  and  $T_{J_{\max}}$  using the procedure outlined in Sec. II D. Figure 6(a) shows a typical supersaturation peak and the corresponding temperature profile as a function of time in the nozzle. In this case, the peak nucleation rate occurs between 67.5 and 70  $\mu\text{s}$  downstream of the throat. The nucleation rate equals 10% of  $J_{\max}$  about 14  $\mu\text{s}$  before and 7  $\mu\text{s}$  after the peak rate is reached, and, thus, nucleation is restricted to a rather narrow region in the nozzle.

Using the supersaturation and temperature profiles, we calculated the theoretical nucleation rates in the nozzle predicted by either the classical nucleation theory<sup>44</sup> (CNT) or the modified CNT of Reiss, Katz, and Kegel<sup>45</sup> (RKK). In Fig. 6(b) we observe that even though the absolute nucleation rates predicted by the two theories differ by about four orders of magnitude, the shape of the nucleation curves is almost identical. When we divide the nucleation rates predicted by the RKK theory by a factor of 79 and multiply that predicted by CNT by the same amount, the two curves overlap exactly, and the nucleation volumes predicted by the two theories differ by <1%.

Table VI summarizes the peak nucleation rates as a function of supersaturation and temperature measured in the nozzle. It also includes the values of  $\Delta t_{J_{\max}}$  and  $\rho_{\text{NZ}}/\rho_{\text{VV}}$  used to calculate  $J_{\max}$ . The two values for  $J_{\max}$  given in Table VI correspond to the two independent estimates of the volume fraction of the aerosol. In most cases, the agreement between these two values is quite good. Significant deviation is only observed when onset occurs at the position furthest downstream of the throat, and even here the two values of  $J_{\max}$  are well within a factor of 2.

To estimate the overall uncertainty associated with the nucleation rates, we need to consider the uncertainties in the number density, the characteristic time, and the density change between the nucleation zone and the viewing volume. The uncertainty in the number density stems from the uncer-

TABLE VI. The peak nucleation rates  $J_{\max}(S_{J_{\max}}, T_{J_{\max}})$  are summarized. The values in columns 7 and 8 correspond to the values of  $N$  in columns 6 and 8 in Table V.

$T_0$	$\dot{m}_v$ , g/min	$T_{J_{\max}}$ , K	$p_{v,J_{\max}}$ , Pa	$S_{J_{\max}}$	$\Delta t_{J_{\max}}$ , $\mu$ s	$\rho_{NZ}/\rho_{vv}$	$J_{\max}$ , $\text{cm}^{-3} \text{s}^{-1}$	$J_{\max}$ , $\text{cm}^{-3} \text{s}^{-1}$
25	2.03	208.8	94.4	135	14.7	1.14	$7.91 \times 10^{16}$	$1.17 \times 10^{17}$
	4.50	222.6	254	62.3	9.7	1.32	$7.50 \times 10^{16}$	$7.50 \times 10^{16}$
35	3.26	215.5	154	90.5	13.9	1.12	$6.43 \times 10^{16}$	$9.99 \times 10^{16}$
	5.07	222.9	272	64.3	11.4	1.21	$6.61 \times 10^{16}$	$6.60 \times 10^{16}$
45	7.71	230.0	444	46.5	9.0	1.30	$6.52 \times 10^{16}$	$6.13 \times 10^{16}$
	5.8	222.8	283	67.8	11.9	1.11	$5.77 \times 10^{16}$	$8.11 \times 10^{16}$
	13.2	237.5	772	36.2	8.3	1.30	$6.47 \times 10^{16}$	$6.28 \times 10^{16}$

tainty in fitting the scattering data (the formal error in the fitted parameters is usually much less than 5%), the uncertainty in the absolute calibration factor for the SANS experiments ( $\sim 10\%$ ), the difference between  $\phi_{\text{SANS}}$  and  $\phi_{\text{PT}}$  (usually  $\sim 10\% - 15\%$ ) and our assumption that the aerosol follows a log-normal rather than a Gaussian distribution (usually less than  $\sim 10\% - 15\%$ ). Based on a correlation of  $\Delta t_{J_{\max}}$  with the mass flow rate, the uncertainty in  $\Delta t_{J_{\max}}$  is less than 10%. Finally, although the gas density in the viewing volume changes by a few percent, within this region it is a linear function of position. By using the density at the center of the viewing volume, the variation in density cancels and can be ignored. In the nucleation zone the density varies by about 3% but by using the density corresponding to the maximum nucleation rate conditions, changes in the density again essentially cancel. Our overall estimate for the uncertainty in  $J_{\max}$  is therefore  $\pm 50\%$ .

To estimate the uncertainty in supersaturation, we need to consider both the mass flow rate and temperature measurements. The uncertainty in measuring the mass flow rates is within 5%. The largest contribution to the uncertainty in the supersaturation, comes from the exponential dependence of this quantity on the equilibrium vapor pressure. The latter quantity depends directly on the initial stagnation temperature measurements. Thus the uncertainty in supersaturation is dominated by the assumption that the uncertainty in the true stagnation temperature measurements is  $\pm 1$  K. In all of the experiments the vapor pressure curve used to calculate the supersaturation is that for liquid  $\text{D}_2\text{O}$  developed by Hill, McMillan, and Lee.<sup>46</sup> We have also included the pressure of the condensible corresponding to the maximum nucleation rate  $p_{v,J_{\max}}$  in Table VI because this value is less dependent on the choice of the vapor pressure curve.

Figure 7 illustrates the nucleation rates, calculated using both estimates of  $N$ , as a function of supersaturation and temperature. At higher temperatures, and onset conditions further upstream in the nozzle, the two rate estimates overlap nicely. Even the data taken at  $x = 3.65$  cm have overlapping error bars. The maximum supersaturations we achieved are on the order of 100 and the minimum temperature is below 210 K. For this supersonic nozzle, the nucleation rates appear to be almost independent of the initial conditions or the location of onset. We have also included the single nucleation rate for pure  $\text{D}_2\text{O}$  measured by Heath *et al.*<sup>25</sup> Again, the value agrees well with the current measurements and is well within the experimental error bars.

Finally, the solid lines in Fig. 7 are the nucleation rates

predicted by the empirical correlation function for  $\text{D}_2\text{O}$  developed by Wölk and Strey<sup>36,47</sup> and given by

$$J_{\text{D}_2\text{O}} = J_{\text{BD}} \exp\left(-35.98 + \frac{8.6 \times 10^3}{T}\right), \quad (11)$$

where  $J_{\text{BD}}$  is the Becker–Döring formulation for the classical nucleation rate given by

$$J_{\text{BD}} = \sqrt{\frac{2\sigma}{\pi m}} v_m \left(\frac{p_v}{kT}\right)^2 \exp\left\{\frac{-16\pi v_m^2 \sigma^3}{3(kT \ln S)^3}\right\}. \quad (12)$$

In Eq. (12),  $\sigma$ ,  $v_m$ , and  $m$  are the surface tension of the critical cluster, the molecular volume and mass of the water molecule, respectively, and  $k$  is the Boltzmann constant. Again, the physical property data used to compute these curves are those given in our earlier papers<sup>36,47</sup> and are not repeated here.

Above 215 K, Eq. (11) does a remarkable job of capturing both the supersaturation and temperature dependence of the current data points even though it was developed using data measured solely in the nucleation pulse chamber. Only at temperatures below 215 K does there appear to be a systematic deviation between the predictions of the theory and the rate measurements. We note that at this point classical nucleation theory predicts that the critical cluster contains

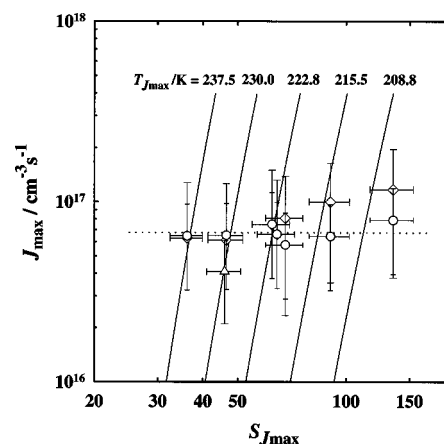


FIG. 7. The peak nucleation rates obtained for our conventional supersonic nozzle are compared to the predictions of the nucleation rate correlation developed by Wölk and Strey (Ref. 36). The circles (diamonds) correspond to the values of  $J_{\max}$  in column 7 (8) of Table VI. The upward facing triangle is the point from Heath *et al.* (Ref. 25).

fewer than 5 molecules and the fundamental assumption that the critical cluster is a compact spherical object is probably unrealistic.

#### IV. CONCLUSIONS

We have made the first direct measurements of nucleation rates in a conventional supersonic nozzle. Our measurements became feasible with the development of the aerosol-SANS technique and our ability to determine the characteristic time for nucleation in the supersonic nozzles. In these monotonically expanding nozzles we rely on the natural nucleation pulse that develops as the gas mixture expands and then condenses rather than enforcing a nucleation pulse by shaping the nozzle. Analyzing the nucleation pulse we found that the characteristic time corresponding to the peak nucleation rate is on the order of 8–14  $\mu$ s, and the shorter pulses correspond to higher mass flow rates. We found that regardless of the initial conditions, the maximum nucleation rate achieved in this particular nozzle appears to be almost a constant. Finally, the current data set shows an amazing consistency with the D<sub>2</sub>O data measured in a nucleation pulse chamber at much lower rates as well as the earlier data point of Heath *et al.*<sup>25</sup>

#### ACKNOWLEDGMENTS

This work was supported by the National Science Foundation, under Grant Nos. CHE-0097896, CHE-0089136, INT-0089897; by the Donors of the Petroleum Research Fund administered by the American Chemical Society; and by the DAAD. We acknowledge the support of the National Institute of Standards and Technology, U.S. Department of Commerce, in providing the facilities used in this work. We thank G. Wilemski and J. Barker for their assistance during the SANS experiments, and Y. Kim and J. Wölk for their comments and help with the figures.

<sup>1</sup>G. M. Pound, *J. Phys. Chem. Ref. Data* **1**, 119 (1972).

<sup>2</sup>R. H. Heist and H. He, *J. Phys. Chem. Ref. Data* **23**, 781 (1994).

<sup>3</sup>A. Laaksonen, V. Talanquer, and D. W. Oxtoby, *Annu. Rev. Phys. Chem.* **46**, 489 (1995).

<sup>4</sup>P. G. Debenedetti, *Metastable Liquids, Concepts, and Principles* (Princeton University Press, Princeton, 1996), p. 148.

<sup>5</sup>J. L. Katz and B. J. Ostermaier, *J. Chem. Phys.* **47**, 478 (1967).

<sup>6</sup>M. M. Rudek, J. L. Katz, and H. Uchtman, *J. Chem. Phys.* **110**, 11505 (1999).

<sup>7</sup>R. H. Heist, J. Ahmed, and M. Janjua, *J. Phys. Chem.* **98**, 4443 (1994).

<sup>8</sup>K. Hameri, M. Kulmala, E. Krissinel, and G. Kodenov, *J. Chem. Phys.* **105**, 7683 (1996).

<sup>9</sup>V. B. Mikheev, N. S. Laulainen, S. E. Barlow, M. Knott, and I. Ford, *J. Chem. Phys.* **113**, 3704 (2000).

<sup>10</sup>H. Lihavainen, Y. Viisanen, and M. Kulmala, *J. Chem. Phys.* **114**, 10031 (2001).

<sup>11</sup>G. W. Adams, J. L. Schmitt, and R. A. Zalabsky, *J. Chem. Phys.* **81**, 5074 (1984).

<sup>12</sup>R. Strey, P. E. Wagner, and Y. Viisanen, *J. Phys. Chem.* **98**, 7748 (1994).

<sup>13</sup>T. Rodemann and F. Peters, *J. Chem. Phys.* **105**, 5168 (1996).

<sup>14</sup>C. F. Lee, "Condensation of H<sub>2</sub>O and D<sub>2</sub>O in argon in the centered expansion wave in a shock tube," in *Condensation in High Speed Flows*, edited by A. A. Pouring (Am. Soc. Mech. Eng., New York, 1977), pp. 83–96.

<sup>15</sup>F. Peters and B. Paikert, *Exp. Fluids* **7**, 521 (1989).

<sup>16</sup>K. N. H. Looijmans and M. E. H. van Dongen, *Exp. Fluids* **23**, 54 (1997), and references therein.

<sup>17</sup>C. C. M. Luitjen, O. D. E. Baas, and M. E. H. van Dongen, *J. Chem. Phys.* **106**, 4152 (1997).

<sup>18</sup>P. P. Wegener and A. A. Pouring, *Phys. Fluids* **7**, 352 (1964).

<sup>19</sup>P. G. Hill, *J. Fluid Mech.* **25**, 593 (1966).

<sup>20</sup>H. L. Jaeger, E. J. Willson, P. G. Hill, and K. C. Russell, *J. Chem. Phys.* **51**, 5380 (1969).

<sup>21</sup>C. A. Moses and G. D. Stein, *J. Fluids Eng.* **100**, 311 (1978).

<sup>22</sup>B. E. Wyslouzil, G. Wilemski, M. G. Beals, and M. B. Frish, *Phys. Fluids* **6**, 2845 (1994).

<sup>23</sup>B. E. Wyslouzil, C. H. Heath, J. L. Cheung, and G. Wilemski, *J. Chem. Phys.* **113**, 7317 (2000).

<sup>24</sup>C. H. Heath, K. A. Streletzky, B. E. Wyslouzil, J. Wölk, and R. Strey, *J. Chem. Phys.* **117**, 6176 (2002).

<sup>25</sup>C. H. Heath, K. A. Streletzky, B. E. Wyslouzil, J. Wölk, and R. Strey, *J. Chem. Phys.* **118**, 5465 (2003).

<sup>26</sup>K. A. Streletzky, Y. Zvinevich, B. E. Wyslouzil, and R. Strey, *J. Chem. Phys.* **116**, 4058 (2002).

<sup>27</sup>P. P. Wegener, "Gas dynamics of expansion flows with condensation and homogeneous nucleation of water vapor," in *Nonequilibrium Flows*, edited by P. P. Wegener (Dekker, New York, 1966), Part I, Vol. 1.

<sup>28</sup>K. Yasuoka and M. Matsumoto, *J. Chem. Phys.* **109**, 8463 (1998).

<sup>29</sup>P. R. ten Wolde, M. J. Ruiz-Montero, and D. Frenkel, *J. Chem. Phys.* **110**, 1591 (1999).

<sup>30</sup>B. Chen, J. I. Siepmann, K. J. Oh, and M. L. Klein, *J. Chem. Phys.* **116**, 4317 (2002).

<sup>31</sup>A. A. Pouring, Ph.D. thesis, Yale University, 1963.

<sup>32</sup>G. D. Stein and P. P. Wegener, *J. Chem. Phys.* **46**, 3685 (1967).

<sup>33</sup>G. D. Stein and C. A. Moses, *J. Colloid Interface Sci.* **39**, 504 (1972).

<sup>34</sup>R. Roberts, "A light scattering investigation of droplet growth in nozzle condensation," Report No. 97, MIT, Gas Turbine Lab, Cambridge, MA, 1969.

<sup>35</sup>C. Heath, B. E. Wyslouzil, and G. Wilemski, AICHE 2000 Annual Meeting, Los Angeles, CA, Nov 15, 2000.

<sup>36</sup>J. Wölk and R. Strey, *J. Phys. Chem. B* **105**, 11683 (2001).

<sup>37</sup>NG3 and NG7 30-meter SANS Instruments Data Acquisition Manual, National Institute of Standards and Technology (NIST NCNR, Rockville, MD, 1999) (Manual).

<sup>38</sup>B. E. Wyslouzil, J. L. Cheung, G. Wilemski, and R. Strey, *Phys. Rev. Lett.* **79**, 431 (1997).

<sup>39</sup>B. E. Wyslouzil, J. L. Cheung, G. Wilemski, R. Strey, and J. Barker, *Phys. Rev. E* **60**, 4330 (1999).

<sup>40</sup>G. Wilemski, *Phys. Rev. E* **61**, 557 (2000).

<sup>41</sup>S. Kline (personal communication, 2001).

<sup>42</sup>V. F. Sears, *Neutron News*, **3**, 29 (1992).

<sup>43</sup>P. E. Wagner and M. Anisimov, *J. Aerosol Sci.* **24s1**, 103 (1993).

<sup>44</sup>R. Becker and W. Döring, *Ann. Phys. (Paris)* **24**, 719 (1935).

<sup>45</sup>H. Reiss, W. K. Kegel, and J. L. Katz, *Phys. Rev. Lett.* **78**, 4506 (1997).

<sup>46</sup>P. G. Hill, R. D. C. McMillan, and V. Lee, *J. Phys. Chem.* **11**, 1 (1982).

<sup>47</sup>J. Wölk, R. Strey, C. H. Heath, and B. E. Wyslouzil, *J. Chem. Phys.* **117**, 4954 (2002).